Pergamon

Int. J. Heat Mass Transfer. Vol. 40, No. 3, pp. 689–698, 1997

0017–9310/97 $15.00+0.00

PII: S0017–9310(96)00137–8

Transient coupled conductive/radiative heat transfer in absorbing, emitting and scattering media: application to laser–flash measurements on ceramic materials

O. HAHN and F. RAETHER

Fraunhofer Institut für Silicatforschung, Neunerplatz 2, D-97082 Würzburg, Germany

M. C. ARDUINI-SCHUSTER

Bayerisches Zentrum für Angewandte Energieforschung, Am Hubland, D-97074 Würzburg, Germany

and

J. FRICKE

Physikalisches Institut der Universität Würzburg, Am Hubland, D-97074 Würzburg, Germany

(*Received* 8 *December* 1995)

Abstract—A model is presented for the calculation of transient combined radiative/conductive heat transfer in heterogeneous semitransparent materials at elevated temperatures. It is based on optical material properties (scattering, absorption) that can be determined experimentally at room temperature. This model is applied to the simulation of laser–flash measurements on ceramic powder compacts. We demonstrate that the relevance of the radiative contributions for the determination of the thermal diffusivity from laser–flash measurements depends on the sample thickness, which is confirmed by corresponding experiments. It is shown that the thermal diffusivity of 1–2 mm thick alumina powder compacts may be overestimated by about 10–20% at 850°C. Copyright © 1996 Elsevier Science Ltd.

1. INTRODUCTION

The laser–flash technique [1] is widely used for thermal diffusivity measurements. The front side of the sample is irradiated by a short laser pulse. The temperature at the back side is monitored using a i.r. detector. The thermal diffusivity is determined from the variation of the temperature at the rear side of the specimen.

In order to get a detectable rear side temperature rise, a sufficient amount of laser energy must be absorbed by the sample. As many samples (e.g. most ceramics) have low emissivities in the wavelength range from 500 nm to 3 μm either a laser, that emits in a region of strong absorption (e.g. a CO_2 laser with $\lambda = 10.6$ μm) must be used, or the samples must be coated with strongly absorbing material (e.g. graphite).

Direct radiative transfer between the sample surfaces as well as radiative interactions between coating and sample can be avoided by coating both sample sides first with a reflecting material (e.g. gold) and then applying an absorbing coating [2]. Although direct radiative transfer between the surfaces can thus be excluded there may still be radiative transport within the sample.

Transient heat transfer for absorbing and emitting media, as reviewed by Viskanta and Anderson [3], has been widely investigated. However, most authors restrict themselves to the treatment of prescribed boundary temperatures. The transient cooldown of a gray absorbing, emitting and scattering medium was investigated by Weston and Hauth [4]. Saulnier [5] treated transient heat transfer in an emitting and absorbing slab irradiated by a heat pulse at one black boundary. He improved Hottel's zonal method [6] for his calculations. He Ping and Lallemand [7] investigated semitransparent slabs with further generalized boundary conditions. Darby [8] showed the importance of radiative heat transfer at elevated temperatures for laser–flash measurements on float glass in a steel–glass–steel layer stack. Maillet *et al.* [9] finally applied the general considerations of He Ping and Lallemand, to calculations concerning the conditions under which laser–flash measurements on float glass are free of radiative contributions.

All the mentioned articles concerning laser–flash measurements only consider absorbing and emitting media. As porous ceramics do not only absorb and emit radiation but also scatter it, we must deal with transient combined conductive/radiative heat transfer in absorbing, emitting and scattering media. As the absorption and scattering properties of these materials

NOMENCLATURE

a_i	weights of Gaussian quadrature
A	see equation (A2)
$bw(\tilde{\mathbf{x}})$	see equation (A6)
c	velocity of light
c_p	specific heat
C	see equation (A3)
d	thickness of sample
e	specific extinction
$\mathrm{erfc}(\tilde{x})$	$\frac{2}{\sqrt{\pi}}\int_x^\infty \mathrm{d}u\,\mathrm{e}^{-u^2}$ (complementary error function)
$fw(\tilde{x})$	see equation (A6)
$f_{0-\lambda}(T)$	$\frac{15}{\pi^4}\int_{c/\lambda k_B T}^\infty \mathrm{d}\zeta \frac{\zeta^3}{\mathrm{e}^\zeta - 1}$ (fractional function of the first kind)
h	Planck constant
$i_\lambda^p(T)$	Planck function (blackbody radiation in wavelength-range $[\lambda, \lambda+\mathrm{d}\lambda]$ at temperature T)
$i_m^p(T)$	Planck function integrated over band m
$I(\tau, \mu)$	intensity of thermal radiation at location τ in direction μ
I_i, $I_\pm$	intensity in discrete directions μ_i
I_L	laser intensity
I_0^{inc}	incoming intensity at front side (blackbody radiation of furnace)
I_1^{inc}	incoming intensity at rear side (blackbody radiation of furnace)
k	absorption coefficient
k_L	absorption coefficient at λ_L
k_B	Boltzmann constant
l	loss factor
n	refractive index
$p(\mu, \mu')$	phase function of scattering $\mu \to \mu'$
q_{rad}	flux of thermal radiation
R_0	reflectivity at front side
R_1	reflectivity at rear side
t	time
Δt	time step
t_L	pulse length of laser
T	temperature [K]
T_f	furnace temperature [K]
T_i^j	temperature [K] at position x_i and time t_j
$\hat{T}_i$, T_i^+	guess for T_i^{j+1}
T_{back}	backside temperature [K]
T_∞	equilibrium temperature rise for adiabatic boundary conditions [K]
T_0	$1-R_0$ = transmission at front side
T_1	$1-R_1$ = transmission at rear side
w	total number of spectral bands
x	position inside the sample
x_i	position of node i
$\tilde{x}$	x/d relative position.

Greek symbols

α	see equation (A4)
$\beta^\pm(\tilde{x})$	see equation (A5)
ε	accuracy for successive under relaxation
θ	polar angle
κ	$\lambda_{cond}/\rho c_p$ = thermal diffusivity
κ_{app}	apparent thermal diffusivity, obtained from simulation (including radiation effects)
κ_{meas}	thermal diffusivity determinated via laser–flash measurement
λ	wavelength
λ_L	wavelength of laser
λ_{cond}	thermal conductivity according to Fourier's law
μ	$\cos\theta$ = directional cosine with respect to the x-axis
μ_i	cosine of discrete direction i
ϕ	$k_L\sqrt{\kappa t_L}$
Φ	azimuthal angle
χ	$k_L x$
ξ'	see equation (A2)
ξ	see equation (A4)
ρ	density
σ_B	Stefan–Boltzmann constant
τ	$e \cdot x$ = optical depth
τ_0	optical thickness of sample
ω	albedo.

Subscripts

λ	at wavelength λ
m	in spectral band m.

Superscripts

*	refers to scaled quantities.

exhibit a strong spectral variation the non-gray case has to be considered.

The paper is organized as follows: first we will outline the theoretical model that we used for our calculations (Section 2) and describe the numerical algorithm (Section 3). The experimental determination of the necessary input parameters is discussed in Section 4. Finally, in Section 5 results will be presented, discussed and compared to experiments.

2. THE THEORETICAL MODEL

2.1. *Solving the equation of radiative transfer*

The spectral intensity of the thermal radiation inside the sample is governed by the one-dimensional equation of radiative transfer [10]

$$\mu \frac{\mathrm{d}}{\mathrm{d}\tau} I_\lambda(\tau,\mu) = \underbrace{-I_\lambda(\tau,\mu)}_{\substack{\text{loss}\\ \text{by}\\ \text{extinction}}} + \underbrace{\frac{\omega}{2}\int_{-1}^{+1} \mathrm{d}\mu' p_\lambda(\mu',\mu) I_\lambda(\tau,\mu')}_{\substack{\text{gain}\\ \text{by}\\ \text{'in-scattering'}}} \underbrace{+(1-\omega) i_\lambda^{\mathrm{P}}(T(\tau))}_{\substack{\text{gain}\\ \text{by}\\ \text{thermal emission}}} \quad (1)$$

with the Planck function

$$i_\lambda^{\mathrm{P}}(T(\tau)) = \frac{n_\lambda^2 4hc^2}{\lambda^5} \frac{1}{\mathrm{e}^{hc/\lambda k_{\mathrm{B}} T(\tau)} - 1} \quad \text{in } [\lambda, \lambda + \mathrm{d}\lambda] \quad (2)$$

as source function (the definition of the directional intensity $I(\tau,\mu)$ is visualised in Fig. 1).

As we are not interested in the exact angular dependence of the intensities but rather in some angle integrated quantities (like the radiative flux), we may simplify (1). The scaling properties of the equation of radiative transfer allow us to apply the so-called δ–0 approximation; that is to choose the unknown phase function to be isotropic, $p_\lambda(\mu,\mu') \equiv 1$, if at the same time we use the scaled albedo ω^* and scaled extinction e^* instead of ω and e. The scaled quantities are correlated to the unscaled ones via the factor of anisotropy g (see ref. [11] for more details).

For numerical reasons we replace the continuous variable λ by discrete 'spectral bands': $m = [\lambda_m, \lambda_{m+1}]$. The source function (2) then becomes

$$i_m^{\mathrm{P}}(T(\tau^*)) \simeq n_m^2 \int_{\lambda_m}^{\lambda_{m+1}} \mathrm{d}\lambda \frac{4hc^2}{\lambda^5} \frac{1}{\mathrm{e}^{hc/\lambda k_{\mathrm{B}} T(\tau^*)} - 1}, \quad (3)$$

where n_m is the arithmetic average of the refractive index over the spectral band m. In the same way we define the Planck-averaged albedo and extinction as

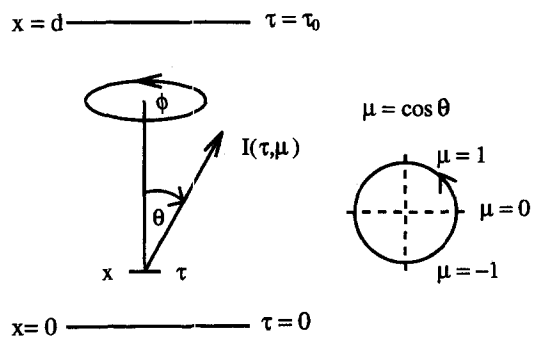

Fig. 1. Definition of the directional intensity $I(\tau,\mu)$. For a one-dimensional infinite slab the directional intensity does not depend on the azimuthal angle Φ.

$$\omega_m^* = \frac{\int_{\lambda_m}^{\lambda_{m+1}} \mathrm{d}\lambda \dfrac{\omega_\lambda^*}{\lambda^5(\mathrm{e}^{hc/\lambda k_{\mathrm{B}} T_{\mathrm{f}}} - 1)}}{\int_{\lambda_m}^{\lambda_{m+1}} \mathrm{d}\lambda \dfrac{1}{\lambda^5(\mathrm{e}^{hc/\lambda k_{\mathrm{B}} T_{\mathrm{f}}} - 1)}},$$

$$e_m^* = \frac{\int_{\lambda_m}^{\lambda_{m+1}} \mathrm{d}\lambda \dfrac{e_\lambda^*}{\lambda^5(\mathrm{e}^{hc/\lambda k_{\mathrm{B}} T_{\mathrm{f}}} - 1)}}{\int_{\lambda_m}^{\lambda_{m+1}} \mathrm{d}\lambda \dfrac{1}{\lambda^5(\mathrm{e}^{hc/\lambda k_{\mathrm{B}} T_{\mathrm{f}}} - 1)}}. \quad (4)$$

For simplicity we will drop the band index in the following, wherever possible. Equation (1) thus looks (for every spectral band):

$$\mu \frac{\mathrm{d}}{\mathrm{d}\tau} I(\tau^*,\mu) = -I(\tau^*,\mu) + \frac{\omega^*}{2}\int_{-1}^{+1} \mathrm{d}\mu' I(\tau^*,\mu') + (1-\omega^*) i^{\mathrm{P}}(T(\tau^*)). \quad (5)$$

No general solution is known for the integro-differential equation (5). An approximate solution can be obtained by the method of discrete ordinates [12]. The integral in (5) is then evaluated by Gaussian quadrature, e.g. it is approximated by a sum

$$\int_{-1}^{+1} \mathrm{d}\mu f(\mu) \approx \sum_{i=1}^{n} a_i f(\mu_i), \quad (6)$$

where in our case $f(\mu) = I(\tau^*,\mu)$. By suitable choice of the discrete directions μ_i and weights a_i a good approximation can be achieved even for small n. One possibility [13] is to choose directions and weights in such a way that the sum actually equals the integral if the integrand is a polynomial of degree $(2n-1)$. Various other prescriptions exist in the literature [11, 12], depending on what one defines as 'good approximation'.

We performed our calculations using the three flux model ($n = 3$) for the following reasons:

- The three flux model gives a better approximation than the two flux model (or Schuster–Schwarzschild approximation [14]), but does not introduce new mathematics.
- As the source function in (5) is isotropic, the integrand is expected not to be strongly anisotropic. Thus it may already be represented satisfactorily by a polynomial of low degree. Comparison of predictions for the radiative flux deduced from the scaled three flux model with Monte-Carlo simulations [15] have shown deviations of at most 10%.
- The input parameters τ^* and ω^* are extracted from diffuse reflectance and transmission measurements using the same δ–0 three flux model (see Section 4).

Invoking the method of discrete ordinates [12] equation (5) can be transformed into a set of coupled differential equations which then can be solved by standard procedures (see Appendix A for more details).

2.2. *Coupling conduction and radiation*

Allowing for radiative heat transfer besides pure conductive heat transfer, the dynamic evolution of the temperature profile in the sample is described by an inhomogeneous diffusion equation:

$$\rho c_p \frac{\partial}{\partial t} T(x,t) - \lambda_{cond} \frac{\partial^2}{\partial x^2} T(x,t) = -\operatorname{div} q_{rad}(x,t). \tag{7}$$

For a porous material, the thermal conductivity λ_{cond} depends, in a complicated way, on the solid phase conductivity, the conductivity of the gas that fills the pore space and the pore space geometry [16].

Thus the divergence of the total radiative flux

$$q_{rad}(x,t) = \int_0^\infty d\lambda\, 2\pi \int_{-1}^{+1} d\mu\, \mu I_\lambda(x,t,\mu) \tag{8}$$

appears as source term in equation (7). An expression for the divergence of the radiative flux can be obtained by overintegrating (1) with $\int_{-1}^{+1} d\mu$ and leads to

$$\operatorname{div} q_{rad}(x,t) = \int_0^\infty d\lambda\, e_\lambda (1-\omega_\lambda) \times \left(\underbrace{4\pi i_\lambda^P(T(x,t))}_{\text{emission}} \underbrace{- 2\pi \int_{-1}^{+1} d\mu I_\lambda(x,t,\mu)}_{\text{absorption}} \right). \tag{9}$$

Explicit expressions for the radiative flux and its divergence within the three flux model are given in Appendix A. The numerical solution of (7) will be discussed in Section 3.

2.3. *Initial temperature distribution*

We used a CO_2 laser at $\lambda_L = 10.6\ \mu m$ with a pulse length of $t_L = 20\ \mu s$ for thermal excitation. As the investigated materials have a large absorption coefficient ($k_L \approx 50\ mm^{-1}$ for alumina) at this wavelength we did not coat them.

The absorption length of many ceramics at λ_L is of the same order of magnitude as the thermal diffusion length during the laser pulse duration t_L. If we want to obtain the correct initial temperature profile we thus can neither treat absorption as a surface process and consider diffusion alone during t_L, nor neglect diffusion and assume the temperature profile to be governed by absorption alone. The combined effect was taken into account by using the Green's function for the diffusion equation [17]:

$$T(x,t_L) = \frac{K_L I_L}{2\rho c_p \sqrt{\kappa\pi}} \int_0^{t_L} du \int_0^\infty dy \frac{1}{\sqrt{u}} \times \left\{ \exp\left(-\frac{(x+y)^2}{4\kappa u} \right) + \exp\left(-\frac{(x-y)^2}{4\kappa u} \right) \right\}. \tag{10}$$

After transforming the integral into a convolution integral [18] and solving it for constant laser intensity I_L during t_L one obtains:

$$T(x,t_L) = \frac{k_L I_L t_L}{2\rho c_p \phi^2} \times \left[e^{(\phi^2+\chi)} \operatorname{erfc}(\phi + \chi/2\phi) + e^{(\phi^2-\chi)} \operatorname{erfc}(\phi - \chi/2\phi) + 2\left(\frac{2}{\sqrt{\pi}} \phi\, e^{-(\chi/2\phi)^2} - \chi \operatorname{erfc}(\chi/2\phi) - e^{-\chi} \right) \right]. \tag{11}$$

3. THE NUMERICAL ALGORITHM

The temperature profile inside the sample is calculated at n discrete positions x_i; $i = 1, \ldots, n$. The time integration is performed iteratively in a modified Cranck–Nicolson scheme. The modification is due to the source term in equation (7). The calculation of this source term requires the evaluation of spatial integrals over the source function $i^P(T(x))$ (see Appendix A). This is done analytically after quadratic interpolation of the $i^P(T(x_i))$. As the source functions depends nonlinearly on T, we use the method of successive underrelaxation for every Crank–Nicolson step $t_j \to t_{j+1}$ in order to find the correct $T(x_i, t_{j+1})$. Details of the numerical algorithm are given in Appendix B.

Because of the strong temperature gradient associated with the initial nonequilibrium temperature distribution, the x_i were chosen very dense ($x_2 - x_1 \simeq d/2000$) near the front side and sparse ($x_n - x_{n-1} \simeq d/20$) near the back side ($n = 50$). As thermal relaxation proceeds faster at early times than at later times, the time steps were incremented exponentially by a factor of $\Delta t_{last}/\Delta t_{first} \simeq 2000$.

Taking the nonequilibrium temperature distribution induced by the laser-pulse as the starting point of the simulation, we observed short range oscillations of the calculated temperature profile near to the front side for the first time steps. These oscillations arise because the initial temperature gradient is very strong and the 'von Neumann' condition

$$\frac{2\kappa\,\Delta t}{(x_{i+1} - x_i)^2} < 1 \tag{12}$$

is violated, even when starting with timesteps as short as $\Delta t = 5\ \mu s$. Although the Crank–Nicolson scheme is stable (the oscillations remain finite), numerical errors might appear which could violate energy conservation or produce wrong heat transfer characteristics. Therefore, we compared our numerical simulation for the case of pure conduction (no radiative transfer) and adiabatic boundaries with the analytical solution for the backside temperature rise (see ref. [19])

$$T_{back}(t) = T_\infty \left\{ 1 + \sum_{k=1}^{\infty} (-1)^k \exp\left(-\frac{k^2 \kappa \pi^2}{d^2} t \right) \right\}. \tag{13}$$

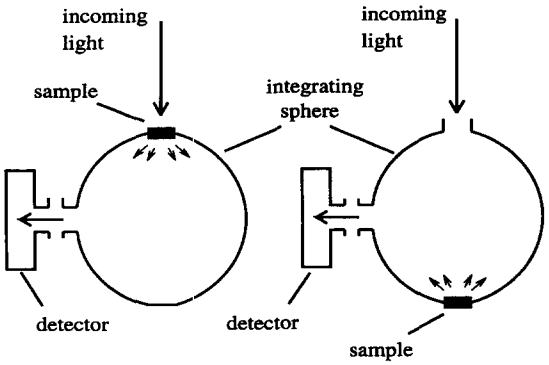

Fig. 2. Experimental setup for measurement of diffuse transmission and reflection. The sample is irradiated on its front side with monochromatic light. The hemispherically diffusely transmitted/reflected radiation is detected by virtue of the integrating sphere.

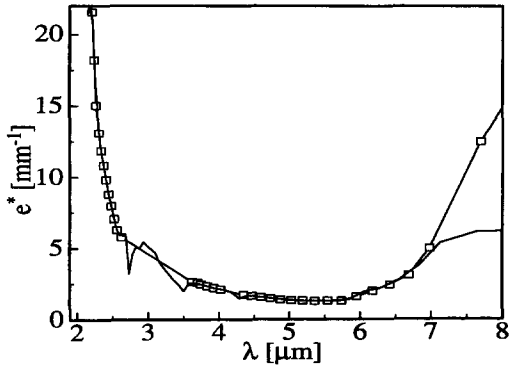

Fig. 3. Scaled specific extinction e^* of pressed alumina powder with 40% porosity. The peaks in the measured extinction (——) between 2.5 and 3.6 μm are due to adsorbed water (humidity of the air) and would thus be absent for a dry sample (□).

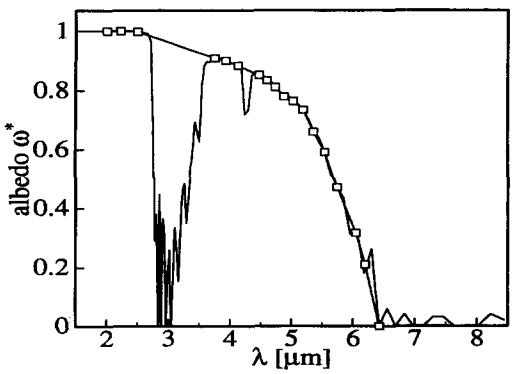

Fig. 4. Scaled albedo ω^* of pressed alumina powder with 40% porosity. The strong absorption peaks exhibited by the measured albedo (——) are due to humidity and would not be present for a dry sample (□).

The relative deviations were smaller than 0.003. Furthermore, we found that these deviations can be reduced by increasing the spatial discretization and thus cannot be attributed to a deficiency of the time integration algorithm. Indeed, simulations with a greater number of timesteps did not improve the deviation. However, a numerical error of 0.003 is acceptable as it is much smaller than the experimental error of the laser–flash method itself.

When switching on radiative transfer, assuming different values for specific extinction and albedo and varying the number of spectral bands, we always obtained the same equilibrium temperature (for reflecting boundaries) as in the case of pure conduction. So the spatial integrals of equation (A6) seem to be well approximated by the method described in Appendix B, otherwise we would expect energy conservation to be violated.

4. EXPERIMENTAL INPUT PARAMETERS

The scattering and absorption properties of the samples were determined by measurement of the hemispherical reflectance and transmission. For this purpose a Bruker IFS 66v infrared spectrometer was used in connection with an integrating sphere in the two configurations depicted in Fig. 2.

We determined the scaled optical depth τ_0^* and albedo ω^* of the samples from the spectral transmission and reflection data within the δ–0 three-flux approximation outlined in Section 2 (see ref. [15] for more details).

Figures 3 and 4 show experimental data for a powder compact.† For low diffusive transmission (<0.02) the determination of τ^* from hemispherical measurements will not be accurate. This is true for $\lambda > 6.5$ μm. However, for $\lambda > 6.5$ μm absorption is the only source of extinction (see Fig. 4). In this region we may thus use the spectral absorption of bulk alumina as measured by Cabannes [20] (the last two data points of the (□) curve are taken from this reference).

As refractive index and absorption coefficient vary with temperature, the obtained spectroscopic data are temperature dependent. However, the experimental determination of hemispherical transmission and reflection is difficult at elevated temperatures.

So we corrected the spectroscopic data obtained at room temperature for higher temperatures under the following assumptions:

(a) for many ceramics the variation of the refractive index with temperature is relatively small and thus may be neglected (e.g. alumina: $\Delta n < 0.002$ for $\Delta T = 100$ K [21]);

(b) the scattering properties of a disperse ceramic material are dominated mainly by the refractive index but less by the absorption coefficient;

(c) the effective absorption coefficient of the disperse material is proportional to the absorption coefficient k of the dense material.

With these assumptions, optical depth and albedo transform from low temperature to high temperature according to

† Alcoa A16SG.

$$(1-\omega^*_{\text{high}})\tau^*_{\text{high}} = \frac{k_{\text{high}}}{k_{\text{low}}}(1-\omega^*_{\text{low}})\tau^*_{\text{low}},$$

$$\omega^*_{\text{high}}\tau^*_{\text{high}} = \omega^*_{\text{low}}\tau^*_{\text{low}}. \quad (14)$$

Although a rigorous proof of the range of validity of (b) and (c) cannot be given because the details of scattering and absorption depend on the unknown microstructure and possibly cannot even be predicted theoretically, the approximate validity of this ansatz may be justified by considering two extreme cases, scattering by pores and scattering by particles.

A highly dense material can be seen as a bulk material with isolated pores. So absorption is only due to the bulk matter between the pores, which themselves do not absorb but only scatter. Thus (b) and (c) are fulfilled.

On the other hand, highly porous materials may be regarded as composed of individual particles. We calculated Mie scattering and absorption cross-section [22] in the wavelength range $\lambda = 1, \ldots, 10$ μm for particle sizes $a = 0.1, \ldots, 20$ μm, absorption coefficients $k = 0.01, \ldots, 500\,\text{cm}^{-1}$ and refractive indices $n = 1.0, \ldots, 2.5$ for $1 < k_{\text{high}}/k_{\text{low}} \leqslant 10$. In general, relation (14) was found to hold within 10%, except for large particles with high absorption at short wavelengths. In this case absorption and extinction are overestimated by the above relation. However, many ceramic materials show high absorption at long wavelengths and low absorption at short wavelengths [20]. Thus equation (14) can be considered a good approximation.

As the assumptions hold in these extreme cases, they are supposed to hold for the true microstructure, which may be seen as an 'intermediate scenario', too.

Radiative transfer is sensitive to the refractive index n due to the quadratic dependence of the Planck function on n (compare equation (2)). We used the spectral refractive index data given in ref. [21]. As we deal with a porous medium the 'effective index of refraction' is neither that of the solid nor that of the gas, which fills the pores. Various effective medium approximations (EMAs) exist predicting n_{eff} for matrices and inclusions of different shapes in the quasistatic limit [23]. However, Aspnes [24] pointed out, that these theories generally tend to underestimate the observed effective refractive index because wave guide mechanisms that appear in finite wavelength theories lead to a concentration of the wave in the medium with higher n. So the correct value of n_{eff} is higher than that deduced from the EMAs.

Lacking a better prescription we have chosen $n_{\text{eff}} = n_{\text{solid}}$ for our calculations and will thus obtain an upper limit for the radiative contributions. Furthermore, we used as input parameters:

- thermal diffusivity κ measured with our laser–flash apparatus;
- c_p from ref. [25];
- variation of spectral absorption coefficient with temperature from ref. [20].

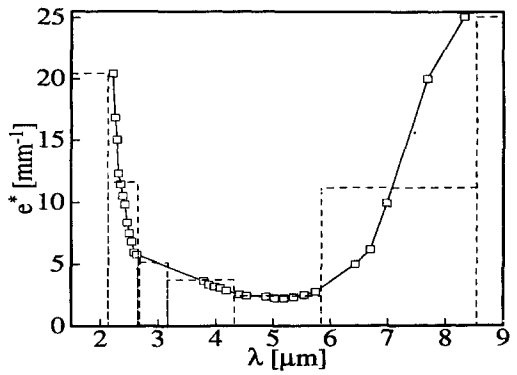

Fig. 5. Scaled specific extinction e^* of pressed alumina powder (□) with 40% porosity, extrapolated to 850°C (compare with Fig. 3) and spectral bands (– – –) for the eight-band-simulation.

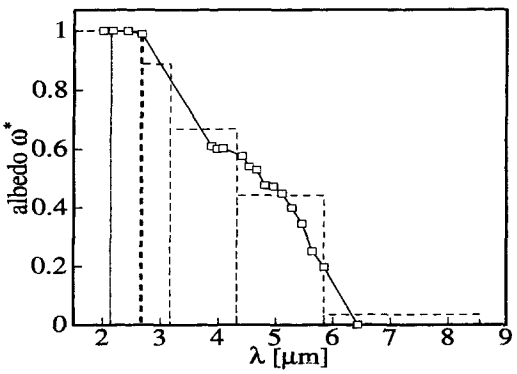

Fig. 6. Scaled albedo ω^* of pressed alumina powder (□) with 40% porosity, extrapolated to 850°C (compare with Fig. 4) and spectral bands (– – –) for the eight-band-simulation.

5. RESULTS AND DISCUSSION

Spectroscopic measurements of the diffuse reflection and transmission were made on ceramic powder compacts as well as on sintered ceramic pellets. These measurements were corrected for the temperature dependence of the absorption as explained in the preceding section. The effect of this correction, when going from ambient temperature to 850°C, is shown in Figs. 5 and 6 for the measurements on alumina powder depicted in Figs. 3 and 4.

In order to check how many spectral bands are necessary to represent the spectral variation of extinction and albedo with sufficient accuracy, we compared an eight-band-simulation and a 16-band-simulation. The results were the same in both cases. So we chose the eight-band-model for all further simulations. A typical run with eight spectral bands from $t = 18$ μs, ..., 2 s needs approximately 3 min on a HP9000/715 workstation (standalone).

For pressed powder compacts non-radiative heat transfer takes place through the solid gas phase. Thus only under vacuum conditions is conductive heat transfer due to phonons alone. The thermal diffusivity

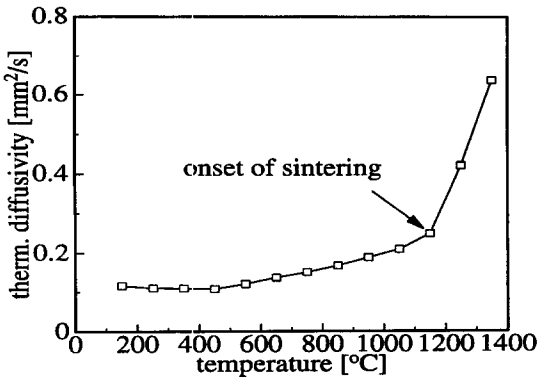

Fig. 7. Thermal diffusivity of an alumina powder compact, measured from room temperature to 1400°C via the laser–flash method [26].

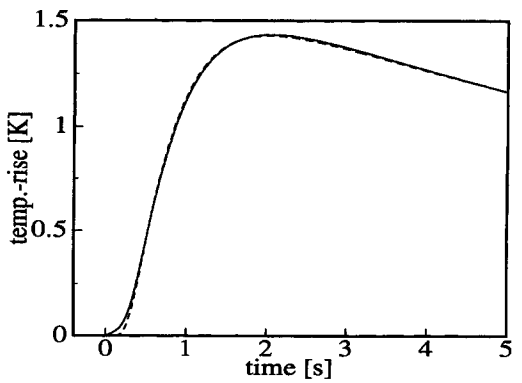

Fig. 8. Numerical simulation of the backside temperature rise (——) for a 1 mm thick sample of pressed alumina powder, including radiative heat transfer. Fitted curve (– – –), assuming no radiative transfer.

data shown in Fig. 7 are taken from ref. [26] and were obtained by laser–flash measurements on a 1 mm thick powder compact, that was heated from room temperature to 1400°C. The contribution to the thermal conductivity of ceramic powders, which is provided by phonons, decreases with increasing temperature (roughly $\propto 1/T$) until the onset of sintering, while heat transfer through the gas phase increases (roughly $\propto \sqrt{T}$) as well as radiative heat transfer ($\propto T^3$). Therefore we expect the interpretation of laser–flash measurements on ceramic powders to be altered most significantly due to radiative heat transfer for temperatures just below the onset of sintering.

In the following, we assume that the conductive heat transfer through solid and gas can be described by an effective thermal diffusivity κ.

From Fig. 7 we see that a thermal diffusivity of $\kappa_{\text{meas}} = 0.167\ \text{mm}^2/\text{s}^{-1}$ was measured at 850°C. This value was obtained by fitting the total experimental backside temperature rise with the analytical solution [19].

$$T_{\text{back}}(t) = 2T_\infty \, \text{d} \sum_{k=1}^{\infty} \beta_k \exp(-\kappa\beta_k^2 t) \times \frac{\beta_k \cos(\beta_k \, \text{d}) + l \sin(\beta_k \, \text{d})}{(\beta_k^2 + l^2)\,\text{d} + 2l}, \quad (15)$$

where β_k are the positive roots of

$$\tan(\beta_k \, \text{d}) = \frac{2\beta_k l}{\beta_k^2 - l^2},$$

which assumes pure conduction but allows for radiative loss at the boundaries. Fit-parameters were the adiabatic equilibrium temperature T_∞, the thermal diffusivity κ and the loss factor l.

Taking $\kappa = 0.145\ \text{mm}^2/\text{s}^{-1}$ as input parameter for the diffusivity we simulated the evolution of the temperature in the sample within a eight-band-model for the optical characteristics given in Figs. 5 and 6. The resulting backside temperature rise was then fitted with equation (15). Both curves are shown in Fig. 8. We observe that the fit-curve almost coincides with the simulated curve for the fit-value of $\kappa_{\text{app}} = 0.167\ \text{mm}^2/\text{s}^{-1}$, but this is just the measured thermal diffusivity, thus a naive interpretation of the laser–flash measurement would lead to overestimate the thermal conductivity by 15%. As the simulated curve is well approximated by the fit-curve, we conclude that radiative contributions cannot be ruled out at first glance from the observation that the measurement yields a 'normally shaped' temperature rise. Repeating the simulation with the same input parameters but for a sample of 2 mm thickness we obtained a deviation of 25%.

From the close agreement of the two curves in Fig. 8, one is tempted to conclude that radiative contributions mainly come from bands of high optical thickness, where the Rosseland diffusion approximation [10] can be applied, yielding $\kappa_{\text{app}} = \kappa + \kappa_{\text{rad}}$. But if this were so, κ_{app} should be independent of the sample thickness.

This dependence can be explained when including contributions from bands of intermediate optical thickness. From equation (7) we know, that for any point inside the sample, the velocity of thermal relaxation due to conduction is proportional to the curvature of the temperature profile at this point. As thermal relaxation progresses, the curvature diminishes and thermal relaxation slows down. On the other hand, using the explicit expression (A8) for the radiative flux and assuming a linear temperature profile in the sample, it can be shown by analytical calculation that even for vanishing curvature of the temperature profile we get $\text{div}\, q_{\text{rad}}(x) \neq 0$ from bands of intermediate optical thickness. So the temperature evolution in the sample will be dominated by conduction for strong curvature and by radiation for weak curvature. As a thick sample needs more time for thermal relaxation than a thin one so, during a longer time, the curvature of the temperature profile in the thick sample is smaller than the one in the thin sample. This

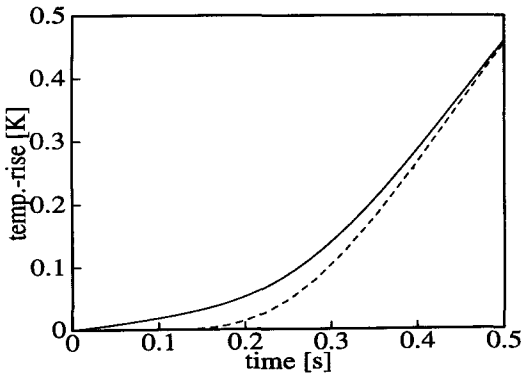

Fig. 9. Detail of Fig. 8, showing deviations between simulation (——) and fit-curve (– – –).

enhances the importance of radiative relaxation for thick samples.

Indeed, a closer look on the curves reveals a trace of the non-diffusive character of radiative transfer in the beginning of the rear side temperature rise (see Fig. 9). Diffusion alone cannot account for the smooth onset of the temperature rise. However, this effect is small and it will hardly be appropriate for discerning radiative transfer experimentally. We conclude that samples should be as thin as possible, if one wants to measure κ because radiative contributions from spectral regions of intermediate optical thickness will then be less important.

We will shortly discuss the influence of some other input parameters. Doubling the laser energy did not show any effect on the apparent thermal diffusivity. Thus the nonlinear dependence of thermal radiation on temperature seems to be negligible and the determination of κ_{app} will remain independent of laser energy as it is in the case of pure conduction. The penetration depth of the laser radiation ($1/k_L$) was found to be irrelevant for the determination of the apparent diffusivity (deviation < 1%), as long as $k_L d > 25$ is guaranteed.

Variation of the boundary conditions, from averaged Fresnel reflection to total reflection, only changed κ_{app} by 2%. This means that radiative contributions will be of the same order of magnitude for gold-coated samples as they are for uncoated samples. This is not true for absorbing coatings, which modify the shape of the backside temperature rise in a different way and thus introduce additional difficulties in the determination of the thermal diffusivity [2].

We emphasize, that the relative importance of radiative transfer for measurements on pressed powders will be enhanced under vacuum conditions due to the diminished κ.

In the case of sintered samples, radiative contributions should be highest at very elevated temperatures for the reasons quoted above. At 1600°C we measured $\kappa_{meas} = 1.28$ mm^2/s^{-1} for a 1 mm thick alumina sample with 2% residual porosity. Using this thermal diffusivity as input parameter for our simulation, we obtained (in the same way as before) an apparent thermal diffusivity of $\kappa_{app} = 1.297$ mm^2/s. The relative error when neglecting radiative effects will thus amount to only 1.3%. Repeating the simulation for a sample of 2 mm thickness we got a deviation of 2.6%. So, for dense alumina, radiative transfer disturbs the measurement of the thermal diffusivity only by a small amount, even at elevated temperatures.

Table 1. Comparison of measured and calculated thermal diffusivities

d [mm]	κ_{meas} [mm^2 s^{-1}]	κ_{app} [mm^2 s^{-1}]
0.777±0.005	0.293±0.005	0.2938
1.292±0.005	0.304±0.006	0.3058
1.800±0.005	0.323±0.010	0.3143
2.309±0.005	0.364±0.011	0.3197

In order to check these theoretical predictions, samples of different thickness d were cut out of an alumina powder compact that was previously tempered at 900°C for 50 h. The pre-tempering ensures that no microstructural changes will take place at temperatures below 900°C, when carrying out the measurements. At room temperature the same thermal diffusivity was measured for all samples ($\kappa_{meas} = 1.140$ mm^2/s^{-1}), but at 850°C the samples showed increasing thermal diffusivity with increasing thickness. In Table 1 the measured diffusivities are compared to numerical simulations assuming $\kappa = 0.2710$ mm^2/s^{-1} as input parameter.

The good agreement between theoretical prediction and experiment for the first three samples justifies the validity of the δ–0 three-flux approximation (Section 2) and the extrapolation scheme for the spectroscopic data (Section 4). The discrepancy for the thickest sample is attributed to radial radiative loss, which is more important for thicker samples than for thinner ones. The samples had a diameter of 11 mm, thus the radial surface of the thick sample already amounts 30% of its total surface.

Although we treated the special case of alumina in the foregoing, the general results of our analysis will be valid for other ceramic materials (e.g. magnesia, zirconia), which possess similar optical properties. However, for a quantitative prediction it is indispensable to repeat the above analysis with the optical and thermal properties of the corresponding material.

6. CONCLUSION

A method for the numerical simulation of transient combined conductive/radiative heat transfer in absorbing, emitting and scattering media is described and used for quantitative simulations of laser–flash measurements.

It is shown how the scattering and absorption properties can be obtained from spectroscopic measurements at room temperature and under which

assumptions these data can be extrapolated to higher temperatures.

Considering alumina powder compacts as an example for materials with low thermal diffusivity it is shown, that laser–flash measurements may lead to a considerable overestimation of the diffusivity. It is found that radiative contributions are less important for thin samples than for thick ones. An explanation for this effect is given, based on the non-local character of radiative interaction and the relaxation properties of diffusive heat transfer. The thickness dependence of the measured thermal diffusivity may serve as an experimental indicator for the presence of appreciable radiative heat transfer from spectral regions of intermediate optical thickness. It is demonstrated, that even if the measured backside temperature rise has the shape of a 'normal' laser–flash measurement, radiative contributions cannot be excluded. For sintered, dense alumina radiative contributions were found to be small, up to 1600°C.

Finally, we would like to remark, that many optical and thermal material properties must be known for a quantitative prediction. Exact knowledge of the spectral dependence of the scaled extinction and albedo in the near infrared is of great importance, as radiative transfer is very sensitive to these data.

Acknowledgements—The authors are indebted to R. Hofmann for performing the laser–flash measurements and for carrying out the backside temperature rise fits. We would like to thank Dr R. Caps and Dr U. Heinemann from the Bayerisches Zentrum für Angewandte Energieforschung, Am Hubland, D-97074 Würzburg for helpful discussions concerning radiative transfer.

REFERENCES

1. W. J. Parker *et al.*, Flash method of determinating thermal diffusivity, heat capacity and thermal conductivity, *J. appl. Phys.* **32,** 1679–1684 (1961).
2. J. Blumm, Bestimmug der Temperaturleitfähigkeit von Ein- und Mehrschichtsystemen mit dem Laserflash-Verfahren. D. thesis, University of Würzbug, Germany (1995).
3. R. Viskanta and E. E. Anderson, Heat transfer in semitransparent solids, *Adv. Heat Transfer* **11,** 317–441 (1975).
4. K. C. Weston and J. L. Hauth, Unsteady, combined radiation and conduction in an absorbing, scattering and emitting medium, *J. Heat Transfer* **95,** 357–364 (1973).
5. J. B. Saulnier, La modélisation thermique et ses applications aux transferts couplés et au contrôle actif. Thèse de Doctorat d'Etat, Université de Poitiers, France (1980).
6. H. C. Hottel and A. F. Sarofim, *Radiative Transfer.* McGraw-Hill, New York (1967).
7. T. He Ping and M. Lallemand, Transient and steady-state combined heat transfer in semi-transparent materials subjected to a pulse or step irradiation, *J. Heat Transfer* **113,** 166–173 (1991).
8. M. I. Darby, Analysis of thermal conductivity experiments on glass at high temperatures, *High Temp. High Press.* **15,** 629–644 (1983).
9. D. Maillet, S. Andre and A. Degiovanni, Heat pulse method and error on measured diffusivity: theory versus experiment, *J. Phys. III* **3,** 883–909 (1993).
10. R. Siegel and J. R. Howell, *Thermal Radiation Heat Transfer.* McGraw-Hill, Tokyo (1990).
11. M. Kaviany, *Principles of Heat Transfer in Porous Media.* Springer, New York (1991).
12. S. Chandrashekar, *Radiation Transfer,* Dover (1960).
13. A. Ishimaru, *Wave Propagation in Random Media I,* p. 205. Academic Press, New York (1978).
14. A. Schuster, Radiation through a foggy atmosphere, *Astrophys. J.* **21,** 1 (1905).
15. R. Caps, Strahlungswärmeströme in evakuierten thermischen superisolationen. Ph.D. thesis, University of Würzburg, Germany (1985).
16. E. Hümmer, M. Rettelbach, X. Lu and J. Fricke, *Thermochim. Acta* **218,** 269–276 (1993).
17. A. Sommerfeld, *Partial Differential Equations in Physics,* p. 49. Academic Press, New York (1949).
18. B. C. H. Wendtland, Temperature in an irradiated thermally conducting translucent medium, *J. Phys. D* **6,** 657–660 (1973).
19. H. S. Carslaw and J. C. Jaeger, *The Conduction of Heat in Solids,* p. 118. Oxford University Press (1976).
20. F. Cabannes, Measurement of infrared absorption of some oxides in connection with the radiative transfer in porous and fibrous materials, *Int. J. Thermophys.* **8,** 97–118 (1987).
21. J. H. Maltison *et al.*, Refractive index of synthetic sapphire, *J. Opt. Soc. Am.* **48,** 72–73 (1958).
22. C. F. Bohren, *Absorption and Scattering of Light by Small Particles,* p. 477. Wiley, New York (1983).
23. W. G. Egan and D. E. Aspnes, Finite-wavelength effects in composite media, *Phys. Rev. B* **26,** 5313–5320 (1982).
24. D. E. Aspnes, Bounds on allowed values of the effective dielectric function of two-component composites at finite frequencies, *Phys. Rev. B* **25,** 1358–1361 (1982).
25. J. D. Cox, D. D. Wagman and V. A. Medvedev, *Key Values for Thermodynamics.* Hemisphere, Washington, DC (1989).
26. F. Raether, R. Hofmann and H. J. Sölter, A new thermo-optical measuring system for the *in situ* monitoring of sintering processes (to be published).
27. D. Schwander, G. Flamant and G. Olalde, Effects of boundary properties on transient temperature distributions in condensed semitransparent media, *Int. J. Heat Mass Transfer* **33,** 1685–1695 (1990).
28. J. Crank and P. Nicolson, A practical method for numerical evaluation of solutions of partial differential equations of the heat-conduction type, *Proc. Camb. Phil. Soc.* **43,** pp. 50–67 (1947).

APPENDIX A. THREE FLUX MODEL

Writing down (5) for the three discrete directions $\mu_0 = 0$, $\mu_2 = -\mu_1$ and inserting (6), the integrodifferential equations decomposes in an algebraic equation for $\mu_0 = 0$ and a set of two coupled linear differential equations for μ_1 and $-\mu_1$. Eliminating I_0 with help of the algebraic equation yields $(I_+ := I_1, I_- := I_2)$:

$$\frac{\mathrm{d}}{\mathrm{d}(\tau^*/\mu_1)}\begin{pmatrix} I_+(\tau^*) \\ I_-(\tau^*) \end{pmatrix} = \begin{pmatrix} A-1 & A \\ -A & -(A-1) \end{pmatrix}\begin{pmatrix} I_+(\tau^*) \\ I_-(\tau^*) \end{pmatrix} + (\xi')^2 \begin{pmatrix} 1 \\ -1 \end{pmatrix} I^{\mathrm{P}}(T(\tau^*)) \quad \text{(A1)}$$

with

$$A = \frac{\omega^* a_1/2}{1-\omega^* a_0/2} \quad \text{and} \quad \xi' = \sqrt{1-2A}. \quad \text{(A2)}$$

The solution of (A1) can be constructed as linear combination of the matrices eigenvectors

$$\begin{pmatrix} I_+(\tau^*) \\ I_-(\tau^*) \end{pmatrix} = \beta^+(\tau^*)\begin{pmatrix} C \\ 1 \end{pmatrix} + \beta^-(\tau^*)\begin{pmatrix} 1 \\ C \end{pmatrix} \quad \text{with } C = \frac{A}{1-A+\xi'}. \tag{A3}$$

The coefficient functions $\beta^{\pm}(\tau^*)$ are solutions of

$$\frac{\mathrm{d}}{\mathrm{d}\tau^*}\beta^{\pm}(\tau^*) = \pm\xi\beta^{\pm}(\tau^*) \mp \alpha i^{\mathrm{P}}(T(\tau^*))$$

$$\text{with } \xi = \frac{\xi'}{\mu_1} \quad \text{and} \quad \alpha = \frac{\xi}{1+C}. \tag{A4}$$

Allowing for reflections at the boundaries one obtains

$$\beta^+(\tilde{x}) = \beta^+(1)\exp(-\xi\tau_0^*(1-\tilde{x})) + bw(\tilde{x})$$

$$\beta^-(\tilde{x}) = \beta^-(0)\exp(-\xi\tau_0^*\tilde{x}) + fw(\tilde{x}), \tag{A5}$$

where

$$fw(\tilde{x}) = \alpha\tau_0^* \int_0^{\tilde{x}} \mathrm{d}\tilde{x}' i^{\mathrm{P}}(T(\tilde{x}'))\exp(-\xi\tau_0^*(\tilde{x}-\tilde{x}'))$$

$$bw(\tilde{x}) = \alpha\tau_0^* \int_{\tilde{x}}^1 \mathrm{d}\tilde{x}' i^{\mathrm{P}}(T(\tilde{x}'))\exp(-\xi\tau_0^*(\tilde{x}'-\tilde{x}))$$

$$\beta^+(1) = \frac{1}{\det M}[M_{22}(T_0 I_0^{\mathrm{inc}} - (C-R_0)bw(0)) - M_{12}(T_1 I_1^{\mathrm{inc}} - (C-R_1)fw(1))]$$

$$\beta^-(0) = \frac{1}{\det M}[-M_{21}(T_0 I_0^{\mathrm{inc}} - (C-R_0)bw(0)) + M_{11}(T_1 I_1^{\mathrm{inc}} - (C-R_1)fw(1))] \tag{A6}$$

and

$$M = \begin{pmatrix} (C-R_0)\exp(-\xi\tau_0^*) & (1-R_0C), \\ (1-R_1C) & (C-R_1)\exp(-\xi\tau_0^*) \end{pmatrix}.$$

Within the three flux model the radiative flux (8) reads

$$q_{\mathrm{rad}}(x,t) = \sum_{m=1}^{w} 2\pi a_1\mu_1[(1-C)(\beta^-(x,t)-\beta^+(x,t))]_m, \tag{A7}$$

while the divergence of the radiative flux (9) yields

$$\operatorname{div} q_{\mathrm{rad}}(x,t) = \sum_{m=1}^{w} 2\pi a_1[e^*(\xi')^2(2i^{\mathrm{P}}(T(x,t)) - (1+C)(\beta^-(x,t)+\beta^+(x,t)))]_m. \tag{A8}$$

So the inhomogeneity of (7), given by (9), is non-local in space (but local in time) as the $\beta^{\pm}(x,t)$ contain spatial integrals over $i_m^{\mathrm{P}}(T(x,t))$.

APPENDIX B. NUMERICAL IMPLEMENTATION

B.1. Spatial integrals

The dynamics of the sample's temperature profile is calculated at n non-equally spaced positions x_i; $i = 1, \ldots, n$. $T(x_1,t)$ is the front side temperature, $T(x_n,t)$ is the rear side temperature. For evaluation of the $\beta^{\pm}(\tilde{x},t)$ we split the integral in (A.5)

$$fw(\tilde{x}_i,t) = \alpha\tau_0^* \int_0^{\tilde{x}_i} \mathrm{d}\tilde{x}' i^{\mathrm{P}}(T(\tilde{x},t))\exp(-\xi\tau_0^*(\tilde{x}_i-\tilde{x}'))$$

$$= \alpha\tau_0^* \sum_{k=1}^{i-1} \int_{\tilde{x}_k}^{\tilde{x}_{k+1}} \mathrm{d}\tilde{x}' i^{\mathrm{P}}(T(\tilde{x}',t))\exp(-\xi\tau_0^*(\tilde{x}_i-\tilde{x}'))$$

$$bw(\tilde{x}_i,t) = \alpha\tau_0^* \int_{\tilde{x}_i}^1 \mathrm{d}\tilde{x}' i^{\mathrm{P}}(T(\tilde{x}',t))\exp(-\xi\tau_0^*(\tilde{x}'-\tilde{x}_i))$$

$$= \alpha\tau_0^* \sum_{k=i}^{n-1} \int_{\tilde{x}_k}^{\tilde{x}_{k+1}} \mathrm{d}\tilde{x}' i^{\mathrm{P}}(T(\tilde{x}',t))\exp(-\xi\tau_0^*(\tilde{x}'-\tilde{x}_i)) \tag{B1}$$

and approximate $i^{\mathrm{P}}(T(\tilde{x}',t))$ by a polynomial of degree two in the vicinity of $\tilde{x}_i$ and linear in the rest of the sample, e.g.

$$i^{\mathrm{P}}(T(\tilde{x},t)) = \begin{cases} p_i\tilde{x}^2 + q_i\tilde{x} + r_i \text{ in } [\tilde{x}_{i-1}, \ldots, \tilde{x}_{i+1}] \\ q_k\tilde{x} + r_k \text{ in } [\tilde{x}_k, \ldots, \tilde{x}_{k+1}] \quad \text{for } k \neq i-1, i' \end{cases} \tag{B2}$$

where p_i, q_i and r_i are linear combinations of $i^{\mathrm{P}}(T(\tilde{x}_{i-1},t))$, $i^{\mathrm{P}}(T(\tilde{x}_i,t))$ and $i^{\mathrm{P}}(T(\tilde{x}_{i+1},t))$, while q_k and r_k are linear combinations of $i^{\mathrm{P}}(T(\tilde{x}_k,t))$ and $i^{\mathrm{P}}(T(\tilde{x}_{k+1},t))$. This approximation is superior to Hottel's zonal method [6, 27]. Now the integrations in (B.1) can be performed analytically. Rearrangement of the sum finally yields the weights $w_{ik}^{\pm}$:

$$fw(\tilde{x}_i,t) = \alpha\tau_0^* \sum_{k=1}^{i+1} i^{\mathrm{P}}(T(\tilde{x}_k,t))w_{ik}^+$$

$$bw(\tilde{x}_i,t) = \alpha\tau_0^* \sum_{k=i-1}^{n} i^{\mathrm{P}}(T(\tilde{x}_k,t))w_{ik}^-. \tag{B3}$$

B.2. SUR and time iteration

The time integration was performed iteratively. A modified Crank–Nicolson method [28] was used, as it is second-order accurate in space and time. This finite difference method is the arithmetical average of an explicit and a fully implicit scheme, e.g. (7) is replaced by

$$\rho c_p \frac{T(x,t_{j+1}) - T(x,t_j)}{t_{j+1}-t_j} - \frac{\lambda_{\mathrm{cond}}}{2}\left(\frac{\partial^2}{\partial x^2}T(x,t_{j+1}) + \frac{\partial^2}{\partial x^2}T(x,t_j)\right) = -\frac{1}{2}(\operatorname{div} q_{\mathrm{rad}}(x,t_{j+1}) + \operatorname{div} q_{\mathrm{rad}}(x,t_j)). \tag{B4}$$

After finite differencing the diffusion term, inserting (B3) in (A5) and using the expansion given in equation (9), the above equation could be rewritten as an inhomogeneous system of linear equations for the unknown $T_i^{j+1} := T(x_i,t_{j+1})$ and therefore be solved, if $i^{\mathrm{P}}(T)$ were a linear function of T.

In order to solve the nonlinear system we first express $i^{\mathrm{P}}(T_i^{j+1})$ as

$$i_m^{\mathrm{P}}(T) = \frac{\sigma_{\mathrm{B}}}{\pi}(f_{0-\lambda_{m+1}}(T) - f_{0-\lambda_m}(T))T^4, \tag{B5}$$

where $f_{0-\lambda}(T)$ can easily be evaluated by a series expansion [10] and then expand T^4 in a Taylor series around a fixed $\hat{T}$:

$$T^4 \approx 4\hat{T}^3T - 3\hat{T}^4. \tag{B6}$$

Finally we obtain

$$i_m^{\mathrm{P}}(T_i^{j+1}) \approx i_m^{\mathrm{P}}(T_i^{j+1},\hat{T}_i) = \frac{\sigma_{\mathrm{B}}}{\pi}(f_{0-\lambda_{m+1}}(\hat{T}_i) - f_{0-\lambda_m}(\hat{T}_i)) \times (4(\hat{T}_i)^3T_i^{j+1} - 3(\hat{T}_i)^4). \tag{B7}$$

Note that this approximation actually gives the exact value for $\hat{T}_i = T_i^{j+1}$. With this linearization an approximation $\hat{T}_i^+$ for the T_i^{j+1} can now be calculated from (B4) for given $\hat{T}_i$. The correct T_i^{j+1} are then found (for every time step $j \to j+1$) by SUR (successive under relaxation), that is: (a) $\hat{T}_i = T_i^j$ is taken as initial guess; (b) $\hat{T}_i^+ = f(T_i^j,\hat{T}_i)$ are calculated from (B4); (c) $\hat{T}_i$ is replaced by $\hat{T}_i^+$; (d) Step (b) and (c) are repeated until $|\hat{T}_i^+ - \hat{T}_i| < \varepsilon$; (e) $T_i^{j+1} := \hat{T}_i^+$ is found. In practice only few iterations were necessary for $\varepsilon = 10^{-5}$ K.